Probing the core of the strong nuclear interaction

https://doi.org/10.1038/s41586-020-2021-6

Received: 21 August 2019

Accepted: 10 January 2020

Published online: 26 February 2020

Check for updates

A. Schmidt[1,2], J. R. Pybus[1], R. Weiss[3], E. P. Segarra[1], A. Hrnjic[1], A. Denniston[1], O. Hen[1]✉, E. Piasetzky[4], L. B. Weinstein[5], N. Barnea[3], M. Strikman[6], A. Larionov[7], D. Higinbotham[8] & The CLAS Collaboration*

The strong nuclear interaction between nucleons (protons and neutrons) is the effective force that holds the atomic nucleus together. This force stems from fundamental interactions between quarks and gluons (the constituents of nucleons) that are described by the equations of quantum chromodynamics. However, as these equations cannot be solved directly, nuclear interactions are described using simplified models, which are well constrained at typical inter-nucleon distances[1–5] but not at shorter distances. This limits our ability to describe high-density nuclear matter such as that in the cores of neutron stars[6]. Here we use high-energy electron scattering measurements that isolate nucleon pairs in short-distance, high-momentum configurations[7–9], accessing a kinematical regime that has not been previously explored by experiments, corresponding to relative momenta between the pair above 400 megaelectronvolts per c (c, speed of light in vacuum). As the relative momentum between two nucleons increases and their separation thereby decreases, we observe a transition from a spin-dependent tensor force to a predominantly spin-independent scalar force. These results demonstrate the usefulness of using such measurements to study the nuclear interaction at short distances and also support the use of point-like nucleon models with two- and three-body effective interactions to describe nuclear systems up to densities several times higher than the central density of the nucleus.

The binding of nucleons (N) in nuclei disrupts the relationship between their mass, m_N, energy, ϵ, and momentum, p, such that $\epsilon^2 \neq (m_N c^2)^2 + (pc)^2$. Therefore, describing atomic nuclei requires modelling the interactions of 'off-shell' nucleon pairs and triplets. Modern models of the nuclear interaction, however, are primarily constrained by free (on-shell) nucleon–nucleon (NN) scattering data.

Occasionally, nucleon pairs at a short distance interact strongly, leading to very high momentum and nucleons that are correspondingly highly off-shell. These naturally occurring high-density fluctuations are called short-range correlations (SRCs)[7–9]. We endeavour to test whether modern NN interaction models can be used effectively to describe the interaction of these highly off-shell nucleons.

To this end, we measured large momentum-transfer electron scattering from a range of nuclei, studying events where the electron, e, scatters quasielastically from a bound nucleon, with either one or two protons, p, detected in coincidence with the scattered electron, e'. These reactions are written as A(e, $e'p$) and A(e, $e'pp$) for one and two protons, respectively; where in our experiment A stands for ^{12}C, ^{27}Al, ^{56}Fe, ^{208}Pb. (Fig. 1 shows a schematic of the two-proton knockout reaction.) These measurements are done in kinematical conditions dominated by the hard breakup of SRC pairs.

Our main observation is that in all measured nuclei—carbon, aluminium, iron and lead—the extracted fraction of proton–proton (pp) SRC pairs increases linearly from nucleon momenta of about 400 to about 650 MeV/c, and then appears to level off. This indicates a transition from a spin-dependent (tensor) to a spin-independent (scalar) NN interaction at high momenta. This transition is also observed in NN interaction models based on either phenomenological or chiral effective field theory (χEFT), provided that they include a tensor interaction.

The good agreement of the calculations with our data confirms the scalar nature of the NN interaction at very high momenta and validates the use of point-like nucleons with effective interactions for modelling the nuclear interaction. This holds true even where the NN interaction is not directly constrained because the nucleons are highly off-shell.

Electron scattering SRC studies

Electron scattering is well described by single-photon exchange[7–14], where electrons scatter from the nucleus by transferring a single virtual photon with momentum $\mathbf{q}$ and energy ω. In the high-resolution one-body view of quasielastic scattering at large momentum transfer, this virtual photon is absorbed by a single off-shell nucleon with initial energy ϵ_i and initial momentum $\mathbf{p}_i$.

If the nucleon does not re-interact as it leaves the nucleus, it will emerge with momentum $\mathbf{p}_N = \mathbf{p}_i + \mathbf{q}$ and energy $\epsilon_N = \omega + \epsilon_i$. Outgoing-nucleon rescattering from other nucleons can change the detected

[1]Massachusetts Institute of Technology, Cambridge, MA, USA. [2]The George Washington University, Washington, DC, USA. [3]Hebrew University, Jerusalem, Israel. [4]Tel Aviv University, Tel Aviv, Israel. [5]Old Dominion University, Norfolk, VA, USA. [6]Pennsylvania State University, University Park, PA, USA. [7]Frankfurt Institute for Advanced Studies, Giersch Science Center, Frankfurt, Germany. [8]Thomas Jefferson National Accelerator Facility, Newport News, VA, USA. *A list of participants and their affiliations appears at the end of the paper. ✉e-mail: hen@mit.edu

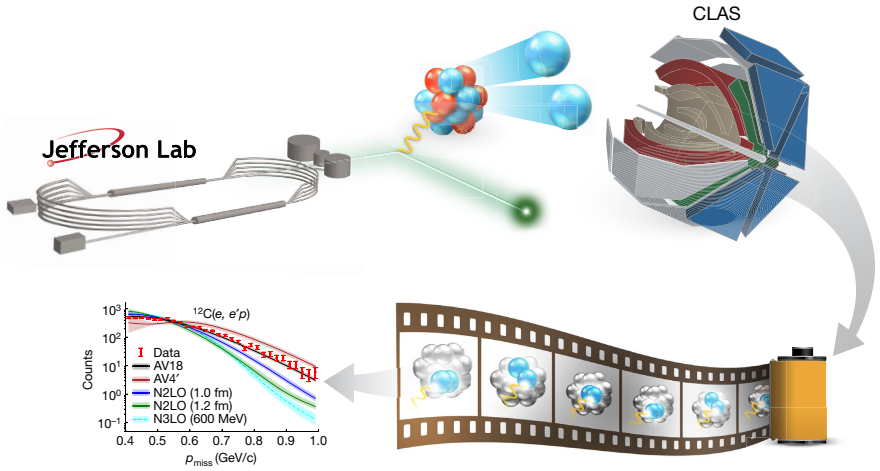

Fig. 1 | Using electron scattering measurements to test the nuclear interaction. 5-GeV electrons from the Jefferson Lab accelerator (top left) impinge on nuclei and break apart SRC nucleon pairs (top middle). The CLAS spectrometer (top right) is used to detect the scattered electrons (green spheres) and knockout protons (blue spheres), which enables the reconstruction of their initial state inside the nucleus. By combining many such observations, the distribution of such pairs inside the nucleus is assembled and compared to theoretical calculations using different models of the strong nuclear interaction. Bottom left, representative data reproduced from Extended Data Fig. 8.

momentum and energy. However, we can still approximate the initial momentum and energy of that nucleon as the measured missing momentum $\mathbf{p}_{miss} = \mathbf{p}_N - \mathbf{q} \approx \mathbf{p}_i$ and missing energy $E_{miss} \equiv \omega - T_N \approx m_N - \epsilon_i$ (where $T_N = \epsilon_N - m_N$ is the kinetic energy of the detected nucleon).

Unlike nucleons in SRC pairs, almost all non-SRC nucleons in atomic nuclei occupy momentum states up to the nuclear Fermi momentum k_F (approximately equal to 250 MeV/c). Therefore, when $p_{miss} > k_F$ ($p_{miss} = |\mathbf{p}_{miss}|$), the knockout nucleon should predominantly originate from an SRC pair and should be accompanied by the simultaneous emission of the other (recoil) nucleon with momentum[10–13,15,16] $\mathbf{p}_{recoil} \approx -\mathbf{p}_i$ (see Extended Data Fig. 1).

Previous A(e, $e'p$) studies observed that more complicated (non-quasielastic) reaction mechanisms can lead to high-p_{miss} events that are not a result of the knockout of nucleons from SRC pairs. To minimize such contributions, our measurement was performed at kinematics where these non-SRC contributions were shown to be suppressed[8,17–19], namely: the momentum transfer squared, $Q^2 \equiv \mathbf{q}^2 - \omega^2 \gtrsim 1.5$ GeV$^2/c^2$, and the Bjorken scaling variable, $x_B \equiv Q^2/(2m_N\omega) \geq 1.2$, so that $\mathbf{p}_{miss}$ was almost anti-parallel to $\mathbf{q}$, and Q^2 grows with $\mathbf{p}_{miss}$. See Methods for details.

Previous measurements of A(e, $e'pN$) reactions off ^{4}He and ^{12}C, performed at similar kinematics, have shown that proton–neutron (pn) SRC pairs predominate over pp SRC pairs for $300 < p_{miss} < 600$ MeV/c by a factor of almost 20 (refs. [10–13,15]). This is due to the dominance of the tensor part of the NN interaction in this momentum range. The tensor force only operates on spin-1 NN pairs. As spin-1 pp SRC pairs are suppressed by the Pauli exclusion principle, there are far more pn pairs than there are pp SRC pairs[7,8,17].

At higher missing-momentum values, where the repulsive core of the NN interaction is expected to become dominant, the interaction should be predominantly scalar; that is, it should operate on both spin-0 and spin-1 pairs. This transition should therefore lead to an increased fraction of pp SRC pairs. Previous work[11] saw initial evidence for such an increase, but the data were statistically limited.

Here we extend these studies by measuring the A(e, $e'p$) and A(e, $e'pp$) reactions for $400 \leq p_{miss} \leq 1{,}000$ MeV/c for ^{12}C, ^{27}Al, ^{56}Fe and ^{208}Pb nuclei. The measurements were performed at the Thomas Jefferson National Accelerator Facility using a 5.01-GeV electron beam. The CEBAF Large Acceptance Spectrometer (CLAS; Fig. 1)[20] was used to detect and identify the scattered electron and knockout protons and reconstruct their momenta; see Methods for details.

We selected (e, $e'p$) events by considering all measured events with a scattered electron with $x_B \geq 1.2$ and a 'leading' proton (momentum p_N) detected within a narrow cone of 25° around the momentum transfer vector $\mathbf{q}$, carrying at least 60% of the transferred momentum ($p_N/q > 0.6$; $q = |\mathbf{q}|$), and resulting in $400 \leq p_{miss} \leq 1{,}000$ MeV/c. (e, $e'pp$) events are a subset of (e, $e'p$) events in which a second 'recoil' proton is detected with momentum greater than 350 MeV/c. This recoil proton has much smaller momenta and a much wider angular distribution than the high-momentum leading proton. See Extended Data Figs. 2–5 for selected kinematical distributions of the measured (e, $e'p$) and (e, $e'pp$) events.

Cross-section modelling

To quantitatively relate observations to the underlying nuclear interaction, we need to calculate the nucleon knockout cross-section starting directly from the NN interaction.

At the high-Q^2 kinematics of our measurement, the differential A(e, $e'p$) nucleon knockout cross-sections can be approximately factorized as[14,21]

$$\frac{d^6\sigma}{d\Omega_{\mathbf{k}'} d\epsilon'_k d\Omega_{\mathbf{p}_N} d\epsilon_N} = p_N \epsilon_N \sigma_{ep} S(\mathbf{p}_i, \epsilon_i) \quad (1)$$

where $\Omega_{\mathbf{k}'}$ and $\Omega_{\mathbf{p}_N}$ are the scattered electron and knockout proton solid angles, $\mathbf{k}'$ ($\mathbf{p}_N$) and ϵ'_k (ϵ_N) are the final electron (proton) momentum and energy, σ_{ep} is the off-shell electron–proton cross-section[21] and $S(\mathbf{p}_i, \epsilon_i)$ is the nuclear spectral function that defines the probability for finding a nucleon in the nucleus with[22] momentum $\mathbf{p}_i$ and energy ϵ_i. Different models of the nuclear interaction can produce different spectral functions, making the measured cross-sections sensitive to the nuclear interaction model.

This commonly used approximation only considers the case in which the virtual photon couples to a single nucleon, described using a one-body reaction operator. However, the full cross-section also has contributions from many-body operators in which the virtual photon couples to more than one nucleon. The contribution of this latter interaction depends on the NN interaction model used in the calculation and is very hard to calculate. However, comparisons between experimental data and this model can indicate the size of the many-body contributions in different kinematical regimes, which can be later quantified by more detailed calculations.

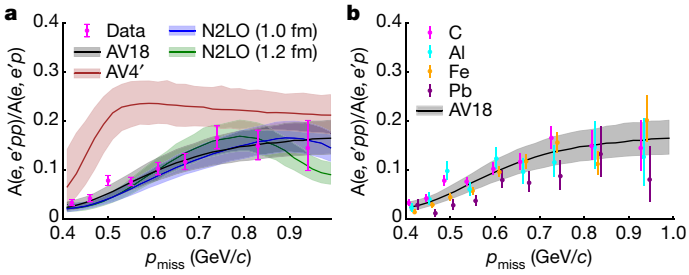

Fig. 2 | Dependence of the two- to one-proton knockout reaction yield ratio on the missing momentum. Measured $(e, e'pp)/(e, e'p)$ event yield values shown as a function of the $(e, e'p)$ missing momentum p_{miss}. **a**, ^{12}C data compared with theoretical calculations based on the GCF framework using different models of the *NN* interaction. **b**, Comparison of the carbon, aluminium, iron and lead data and the GCF AV18 ^{12}C calculation (the latter is reproduced from **a**). In both **a** and **b**, the width of the bands and the data error bars show the systematic uncertainties of the model and the statistical uncertainties of the data, respectively, each at the 1σ confidence level.

The two-nucleon knockout cross-section can be factorized similarly to equation (1) by replacing the single-nucleon spectral function with the two-nucleon decay function that defines the probability of finding nucleons with momenta $\mathbf{p}_i$ and $\mathbf{p}_{recoil}$ such that the system of $A-1$ nucleons (the $A-2$ nucleus plus the recoil proton; A, atomic mass of nucleus A) has energy E_r (refs. [9,15,17]). See Supplementary Information for details.

Ab initio many-body calculations of the nuclear spectral and decay functions are currently computationally unfeasible[1]. However, for the specific case of interacting with SRC pairs (that is, $p_i \approx p_{miss} > k_F$), we can efficiently approximate these functions using the generalized contact formalism (GCF)[22–25] which assumes that at very high momenta, the nuclear wavefunction can be described as consisting of an SRC pair and a residual $A-2$ system. The abundance of SRC pairs is given by nuclear contact terms extracted from ab initio many-body calculations of pair momentum distributions[24,25].

Therefore, in the GCF, the high-momentum proton spectral function of equation (1) is approximated by a sum over *pp* and *pn* SRC pairs, which enables the calculation of the cross-sections of $(e, e'p)$ and $(e, e'pp)$ using different nuclear interaction models as input[13,22].

We consider two commonly used *NN* interaction models: the phenomenological Argonne V18 (AV18)[4] and the χEFT local next-to-next-to-leading-order (N2LO)[5] interactions, as well as the simplified, tensor-less, Argonne V4′ (AV4′) interaction. The χEFT potentials considered here include explicit cut offs at distances of 1.0 fm and 1.2 fm, corresponding to momentum cut offs of about 400–500 MeV/c (ref. [26]). We do not expect these interactions to work well above this cut off (see Methods for details).

We compared the GCF cross-sections to experimental data using Monte Carlo integration, accounting for the acceptance, resolution and residual reaction effects (radiation, transparency and single-charge exchange) of CLAS. The systematic uncertainty of the calculation was estimated by varying the GCF and detector model parameters. See Methods for details on the GCF model and its implementation.

Measurement results

Figure 2 shows the measured $(e, e'pp)/(e, e'p)$ event yield ratio as a function of p_{miss} for carbon, aluminium, iron and lead. The ratio increases linearly from 400 to about 650 MeV/c and then appears to flatten out for all measured nuclei. The observed increase in this ratio—that is, the

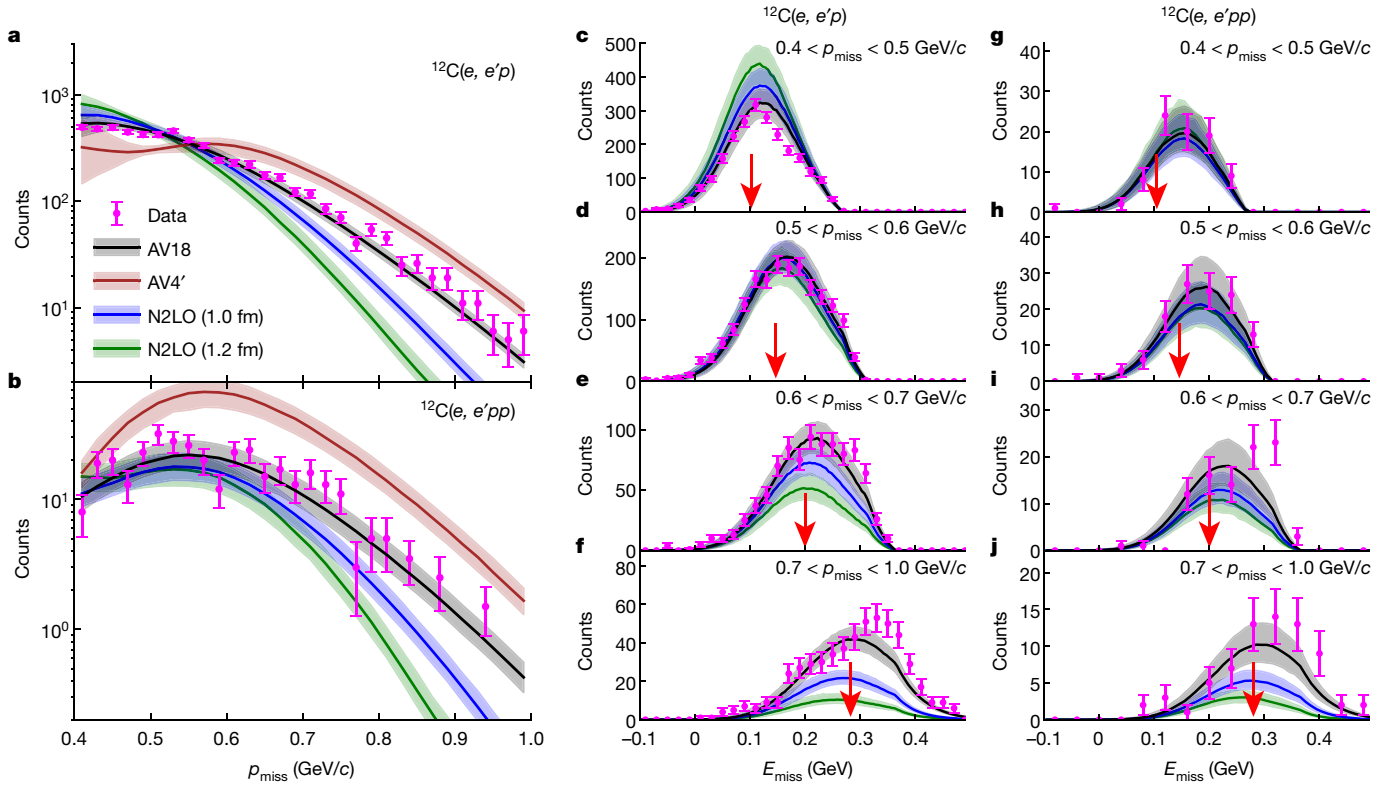

Fig. 3 | Missing-momentum and energy dependence of one- and two-proton knockout reaction yields. a–j, Measured ^{12}C$(e, e'p)$ (**a**, **c**–**f**) and ^{12}C$(e, e'pp)$ (**b**, **g**–**j**) event yields shown as a function of the $(e, e'p)$ missing momentum (**a**, **b**) and missing energy (**c**–**j**). The data are compared with theoretical calculations based on the GCF framework, using different models of the *NN* interaction. The arrows mark the expected missing energy for interacting with a stationary pair with relative momentum equal to the mean of each missing-momentum bin. The width of the bands and the data error bars show the systematic uncertainties of the model and the statistical uncertainties of the data, respectively, each at the 1σ confidence level.

fraction of $(e,e'p)$ events with a recoil proton—is qualitatively consistent with the expected transition from a predominantly tensor interaction to a predominantly scalar interaction at high p_{miss}.

For ^{12}C, the measured ratio is compared with GCF calculations using the AV18 and N2LO interactions, which are in excellent agreement with the data. The scalar-only AV4′ interaction (that which lacks the tensor force) agrees with data in the scalar-dominated high-momentum region but fails in the tensor-dominated low-momentum region.

At high momenta all calculations predict a *pp* SRC pair fraction of about 1/3 (Extended Data Fig. 6c), which is equal to the scalar limit obtained by simple pair counting (see calculation in Methods). This value of 1/3 is then reduced experimentally by the CLAS acceptance and residual reaction effects.

Figure 3 shows the absolute measured and calculated $^{12}C(e,e'pp)$ and $^{12}C(e,e'p)$ yields as a function of p_{miss} and as a function of E_{miss} for different bins in p_{miss}. The average value of E_{miss} increases with p_{miss}, peaking at the expected value for the breakup of an SRC pair at rest, marked by a red arrow in Fig. 3; see equation (3) (in Methods). This supports our interpretation that the measured process is dominated by interaction with an SRC pair, and that the $A-2$ residual system is a spectator[27].

The GCF calculations follow the same trend as the data. The AV18 interaction agrees with the data over the entire E_{miss} and p_{miss} range. The simplified AV4′ interaction, as expected, does not describe the momentum distributions well. The N2LO interactions describe the data well up to about 600 MeV/c. The latter observation is surprising, because the χEFT cut off truncates the *NN* interaction quite severely, leading to very large expected uncertainties already at the cut-off scale. The fact that interactions studied here use a position-space regulator makes their truncation effects considerable at a high momentum scale of 600–700 MeV/c.

For $p_{miss} > 600$ MeV/c the χEFT calculations disagree with the individual $^{12}C(e,e'pp)$ and $^{12}C(e,e'p)$ yields, as expected. However, this disagreement largely cancels in the $(e,e'pp)/(e,e'p)$ yield ratio, indicating that such ratios are good observables that are sensitive to the operator structure of the *NN* interaction.

We therefore use the value of $(e,e'pp)/(e,e'p)$ to extract the relative abundance of *np*/*pp* SRC pairs (that is, the contact term ratios) by fitting the contacts in the GCF calculation to the data (see Methods for details). The resulting contact ratios are listed in Extended Data Table 1. The carbon contact ratios are consistent with those extracted from ab initio calculations[24,25] and the ratios of heavier nuclei relative to ^{12}C are observed to be model-independent quantities, as expected[25].

Extended Data Figs. 3 and 4 show good agreement between the data and the GCF calculation for various other kinematical distributions.

The agreement between the data and the AV18-interaction-based calculations corroborates the validity of the assumptions made in the GCF model, namely the dominance of the interaction of an SRC nucleon pair with the electron via a one-body current operator. On the other hand, we stress that the disagreement we find at higher momentum between the χEFT-based calculations and the data does not necessarily indicate a problem with the *NN* interaction. As the theoretical cross-section is sensitive to both the nuclear interaction and the current operator, the shortcomings of the calculations might be attributed to two-body currents. Additionally, the approximations made in the GCF model (for example, the neglect of three-body SRCs), may explain some of the disagreement.

Two additional tests confirm the suppression of non-quasielastic reaction mechanisms: (1) the $A(e,e'p)$ and $A(e,e'pp)$ p_{miss} and E_{miss} distributions for the nuclei from carbon to lead are identical within uncertainties, indicating the suppression of A-dependent non-quasielastic reaction mechanisms; and (2) the distribution of the kinematical variables that are most sensitive to non-quasielastic reaction mechanisms—such as the angle between $\mathbf{p}_{miss}$ and $\mathbf{q}$ (refs. [8,17,19])—are well described by the GCF-based simulation; see Extended Data Fig. 3 and Supplementary Information for details.

Lastly, owing to the high initial momenta of the measured protons, we assessed the possible impact of relativistic effects on the nuclear wavefunction in the GCF spectral function. As fully relativistic nuclear potentials and wavefunctions are unavailable, relativistic effects can only be treated in an approximate and model-dependent manner. Here we used the relativistic nuclear light-cone formalism[9], which has been previously used for SRC studies using nucleon knockout reactions[15]; see Supplementary Information for details.

Extended Data Fig. 7 shows relativistic light-cone calculations compared with the same data shown in Fig. 3. The relativistic corrections somewhat reduce the agreement with $(e,e'pp)$ data at lower momenta and considerably improve the agreement of χEFT-based calculations with both $(e,e'p)$ and $(e,e'pp)$ data at higher momenta. This is because, in the kinematics of our measurement, the relativistic treatment reduces the effective relative momenta of the probed *NN* pairs, bringing it closer to the χEFT cut-off scale. This suggests that the importance of two-body operators in χEFT-based calculations at large p_{miss} might be small, and should be studied in future using dedicated relativistic calculations.

Conclusions

The measured value of the $A(e,e'pp)/A(e,e'p)$ cross-section is observed to be nucleus-independent, indicating a transition from behaviour reflecting the tensor character of *NN* pairs to behaviour described by spin-independent correlations at high p_{miss}. The large momentum-transfer electron scattering measurements reported here are thus sensitive to the detailed characteristics of the *NN* interaction at high relative momenta.

The one-body GCF approximation describes the data well up to very high missing momenta, even though the input *NN* interaction models were not directly fit to high-momentum data.

These *NN* interactions result from the quark–gluon structure of nucleons. Measurements of quark distributions in nuclei are often explained by modifying bound-nucleon structure[7,28]. Such modifications were recently associated with the large spatial overlap and large off-shellness of nucleons in SRC pairs[7,29,30]. However, our results suggest that even if such modifications exist, they do not have a substantial impact on the modelling of the *NN* interaction.

Our data also point to the importance of two-body interaction operators and relativistic effects at high momenta and highlight the need for more elaborate theoretical calculations. Combined with forthcoming three-nucleon knockout measurements, such calculations will also allow for future studies of the loosely constrained three-nucleon interaction.

Lastly, our data provide strong support for the use of point-like nucleons with effective interactions for modelling atomic nuclei and dense astrophysical systems such as neutron stars, the outer core of which exceeds the nuclear saturation density under current models.

Online content

Any methods, additional references, Nature Research reporting summaries, source data, extended data, supplementary information, acknowledgements, peer review information; details of author contributions and competing interests; and statements of data and code availability are available at https://doi.org/10.1038/s41586-020-2021-6.

1. Carlson, J. et al. Quantum Monte Carlo methods for nuclear physics. *Rev. Mod. Phys.* **87**, 1067 (2015).
2. Epelbaum, E., Hammer, H. W. & Meißner, U. G. Modern theory of nuclear forces. *Rev. Mod. Phys.* **81**, 1773–1825 (2009).
3. Machleidt, R., Holinde, K. & Elster, C. The Bonn meson-exchange model for the nucleon–nucleon interaction. *Phys. Rep.* **149**, 1–89 (1987).
4. Wiringa, R. B., Stoks, V. G. J. & Schiavilla, R. Accurate nucleon–nucleon potential with charge-independence breaking. *Phys. Rev. C* **51**, 38–51 (1995).

5. Gezerlis, A. et al. Quantum Monte Carlo calculations with chiral effective field theory interactions. *Phys. Rev. Lett.* **111**, 032501 (2013).
6. Lattimer, J. M. & Prakash, M. Neutron star observations: prognosis for equation of state constraints. *Phys. Rep.* **442**, 109–165 (2007).
7. Hen, O., Miller, G. A., Piasetzky, E. & Weinstein, L. B. Nucleon–nucleon correlations, short-lived excitations, and the quarks within. *Rev. Mod. Phys.* **89**, 045002 (2017).
8. Ciofi degli Atti, C. In-medium short-range dynamics of nucleons: recent theoretical and experimental advances. *Phys. Rep.* **590**, 1–85 (2015).
9. Frankfurt, L. & Strikman, M. High-energy phenomena, short-range nuclear structure and QCD. *Phys. Rep.* **76**, 215–347 (1981).
10. Subedi, R. et al. Probing cold dense nuclear matter. *Science* **320**, 1476–1478 (2008).
11. Korover, I. et al. Approaching the nucleon–nucleon short-range repulsive core via the ^{4}He(*e*, *e*′*pN*) triple coincidence reaction. *Phys. Rev. Lett.* **113**, 022501 (2014).
12. Hen, O. et al. (Jefferson Lab CLAS Collaboration). Momentum sharing in imbalanced Fermi systems. *Science* **346**, 614–617 (2014).
13. Duer, M. et al. (CLAS Collaboration). Direct observation of proton–neutron short-range correlation dominance in heavy nuclei. *Phys. Rev. Lett.* **122**, 172502 (2019).
14. Kelly, J. J. Nucleon knockout by intermediate-energy electrons. In *Advances in Nuclear Physics* (eds Negele, J. W. & Vogt, E.) 75–294 (1996).
15. Piasetzky, E., Sargsian, M., Frankfurt, L., Strikman, M. & Watson, J. W. Evidence for the strong dominance of proton–neutron correlations in nuclei. *Phys. Rev. Lett.* **97**, 162504 (2006).
16. Cohen, E. O. et al. (CLAS Collaboration). Center of mass motion of short-range correlated nucleon pairs studied via the *A*(*e*, *e*′*pp*) reaction. *Phys. Rev. Lett.* **121**, 092501 (2018).
17. Frankfurt, L., Sargsian, M. M. & Strikman, M. Recent observation of short range nucleon correlations in nuclei and their implications for the structure of nuclei and neutron stars. *Int. J. Mod. Phys. A* **23**, 2991–3055 (2008).
18. Colle, C., Cosyn, W. & Ryckebusch, J. Final-state interactions in two-nucleon knockout reactions. *Phys. Rev. C* **93**, 034608 (2016).
19. Sargsian, M. M. Selected topics in high energy semi-exclusive electro-nuclear reactions. *Int. J. Mod. Phys. E* **10**, 405–458 (2001).
20. Mecking, B. A. et al. The CEBAF large acceptance spectrometer (CLAS). *Nucl. Inst. Meth. A* **503**, 513–553 (2003).
21. De Forest, T. Off-shell electron–nucleon cross sections: the impulse approximation. *Nucl. Phys. A* **392**, 232–248 (1983).
22. Weiss, R., Korover, I., Piasetzky, E., Hen, O. & Barnea, N. Energy and momentum dependence of nuclear short-range correlations – spectral function, exclusive scattering experiments and the contact formalism. *Phys. Lett. B* **791**, 242–248 (2019).
23. Weiss, R., Bazak, B. & Barnea, N. Generalized nuclear contacts and momentum distributions. *Phys. Rev. C* **92**, 054311 (2015).
24. Weiss, R., Cruz-Torres, R., Barnea, N., Piasetzky, E. & Hen, O. The nuclear contacts and short-range correlations in nuclei. *Phys. Lett. B* **780**, 211–215 (2018).
25. Cruz-Torres, R. et al. *Scale and scheme independence and position–momentum equivalence of nuclear short-range correlations*. Preprint at https://arxiv.org/abs/1907.03658 (2019).
26. Hoppe, J., Drischler, C., Furnstahl, R. J., Hebeler, K. & Schwenk, A. Weinberg eigenvalues for chiral nucleon–nucleon interactions. *Phys. Rev. C* **96**, 054002 (2017).
27. Ciofi degli Atti, C., Simula, S., Frankfurt, L. L. & Strikman, M. I. Two-nucleon correlations and the structure of the nucleon spectral function at high values of momentum and removal energy. *Phys. Rev. C* **44**, 7–11 (1991).
28. Norton, P. R. The EMC effect. *Rep. Prog. Phys.* **66**, 1253–1297 (2003).
29. Kulagin, S. A. & Petti, R. Global study of nuclear structure functions. *Nucl. Phys. A* **765**, 126–187 (2006).
30. The CLAS Collaboration. Modified structure of protons and neutrons in correlated pairs. *Nature* **566**, 354–358 (2019).

The CLAS Collaboration

A. Schmidt[1,2], J. R. Pybus[1], R. Weiss[3], E. P. Segarra[1], A. Hrnjic[1], A. Denniston[1], O. Hen[1], E. Piasetzky[4], L. B. Weinstein[5], N. Barnea[3], M. Strikman[6], A. Larionov[7], D. Higinbotham[8], S. Adhikari[9], M. Amaryan[5], G. Angelini[2], G. Asryan[10], H. Atac[11], H. Avakian[8], C. Ayerbe Gayoso[12], L. Baashen[9], L. Barion[13], M. Bashkanov[14], M. Battaglieri[8,15], A. Beck[1], I. Bedlinskiy[16], F. Benmokhtar[17], A. Bianconi[18,19], A. S. Biselli[20,21], F. Bossù[22], S. Boiarinov[8], M. Brahim[23], W. J. Briscoe[2], W. Brooks[24], V. D. Burkert[8], F. Cao[25], D. S. Carman[8], J. C. Carvajal[9], A. Celentano[15], P. Chatagnon[26], T. Chetry[27], G. Ciullo[13,28], L. Clark[29], E. Cohen[4], P. L. Cole[30,31,32], M. Contalbrigo[13], V. Crede[33], R. Cruz-Torres[1], A. D'Angelo[34,35], N. Dashyan[10], R. De Vita[15], E. De Sanctis[36], M. Defurne[22], A. Deur[8], S. Diehl[25], C. Djalali[37,38], M. Duer[4], M. Dugger[39], R. Dupre[26], H. Egiyan[8], M. Ehrhart[26], A. El Alaoui[24], L. El Fassi[27], P. Eugenio[33], A. Filippi[40], T. A. Forest[31], G. Gavalian[8,41], S. Gilad[1], G. P. Gilfoyle[42], K. L. Giovanetti[43], F. X. Girod[8,13], C. Giuseppe[8,13], D. I. Glazier[29], E. Golovatch[44], R. W. Gothe[38], K. A. Griffioen[12], L. Guo[9], K. Hafidi[23], H. Hakobyan[10,24], C. Hanretty[8], N. Harrison[8], M. Hattawy[5], F. Hauenstein[1,5], T. B. Hayward[12], K. Hicks[37], M. Holtrop[41], Y. Ilieva[2,38], I. Illari[2], D. Ireland[29], B. S. Ishkanov[44], E. L. Isupov[44], D. Jenkins[45], H. S. Jo[46], K. Joo[25], D. Keller[47], M. Khachatryan[5], A. Khanal[9], M. Khandaker[48,54], C. W. Kim[2], W. Kim[46], F. J. Klein[32], I. Korover[4], V. Kubarovsky[8,49], L. Lanza[34], M. Leali[18,19], P. Lenisa[13], I. J. D. MacGregor[29], D. Marchand[26], N. Markov[25], L. Marsicano[15], V. Mascagna[19,50,55], S. May-Tal Beck[1], B. McKinnon[29], M. Mirazita[36], V. Mokeev[8], C. Munoz Camacho[26], B. Mustafa[23], P. Nadel-Turonski[8], S. Nanda[27], S. Niccolai[26], G. Niculescu[43], M. Osipenko[15], A. I. Ostrovidov[33], M. Paolone[11], L. L. Pappalardo[13], R. Paremuzyan[41], K. Park[46,56], E. Pasyuk[8,39], M. Patsyuk[1], Phelps[2], O. Pogorelko[16], J. W. Price[51], Y. Prok[5,47], D. Protopopescu[29], M. Ripani[15], D. Ris[25], Rizzo[34,35], G. Rosner[29], P. Rossi[8,36], F. Sabatié[22], C. Salgado[48], B. Schmookler[1], R. A. Schumacher[21], Y. G. Sharabian[8], U. Shrestha[37], Iu. Skorodumina[38,44], D. Sokhan[29], O. Soto[36], N. Sparveris[11], S. Stepanyan[8], I. I. Strakovsky[2], S. Strauch[2,38], J. A. Tan[46], N. Tyler[38], M. Ungaro[8,49], L. Venturelli[18,19], H. Voskanyan[10], E. Voutier[26], R. Wang[26], D. P. Watts[14], X. Wei[8], M. H. Wood[38,52], N. Zachariou[14], J. Zhang[47], Z. W. Zhao[53] & X. Zheng[47]

[9]Florida International University, Miami, FL, USA. [10]Yerevan Physics Institute, Yerevan, Armenia. [11]Temple University, Philadelphia, PA, USA. [12]College of William and Mary, Williamsburg, VA, USA. [13]INFN, Sezione di Ferrara, Ferrara, Italy. [14]University of York, York, UK. [15]INFN, Sezione di Genova, Genoa, Italy. [16]National Research Center Kurchatov Institute – ITEP, Moscow, Russia. [17]Duquesne University, Pittsburgh, PA, USA. [18]Università degli Studi di Brescia, Brescia, Italy. [19]INFN, Sezione di Pavia, Pavia, Italy. [20]Fairfield University, Fairfield, CT, USA. [21]Carnegie Mellon University, Pittsburgh, PA, USA. [22]IRFU, CEA, Université Paris-Saclay, Gif-sur-Yvette, France. [23]Argonne National Laboratory, Argonne, IL, USA. [24]Universidad Técnica Federico Santa María, Valparaíso, Chile. [25]University of Connecticut, Storrs, CT, USA. [26]Institut de Physique Nucléaire, IN2P3-CNRS, Université Paris-Sud, Université Paris-Saclay, Orsay, France. [27]Mississippi State University, Mississippi State, MS, USA. [28]Università di Ferrara, Ferrara, Italy. [29]University of Glasgow, Glasgow, UK. [30]Lamar University, Beaumont, TX, USA. [31]Idaho State University, Pocatello, ID, USA. [32]Catholic University of America, Washington, DC, USA. [33]Florida State University, Tallahassee, FL, USA. [34]INFN, Sezione di Roma Tor Vergata, Rome, Italy. [35]Università di Roma Tor Vergata, Rome, Italy. [36]INFN, Laboratori Nazionali di Frascati, Frascati, Italy. [37]Ohio University, Athens, OH, USA. [38]University of South Carolina, Columbia, SC, USA. [39]Arizona State University, Tempe, AZ, USA. [40]INFN, Sezione di Torino, Turin, Italy. [41]University of New Hampshire, Durham, NH, USA. [42]University of Richmond, Richmond, VA, USA. [43]James Madison University, Harrisonburg, VA, USA. [44]Skobeltsyn Institute of Nuclear Physics, Lomonosov Moscow State University, Moscow, Russia. [45]Virginia Tech, Blacksburg, VA, USA. [46]Kyungpook National University, Daegu, Republic of Korea. [47]University of Virginia, Charlottesville, VA, USA. [48]Norfolk State University, Norfolk, VA, USA. [49]Rensselaer Polytechnic Institute, Troy, New York, NY, USA. [50]Università degli Studi dell'Insubria, Como, Italy. [51]California State University, Dominguez Hills, Carson, CA, USA. [52]Canisius College, Buffalo, NY, USA. [53]Duke University, Durham, NC, USA. [54]Present address: Idaho State University, Pocatello, ID, USA. [55]Present address: Università degli Studi di Brescia, Brescia, Italy. [56]Present address: Thomas Jefferson National Accelerator Facility, Newport News, VA, USA.

Methods

CLAS detector and particle identification

CLAS was a six-sector toroidal magnetic spectrometer[20]. Each sector was equipped with three layers of drift chambers, time-of-flight scintillation counters, Cerenkov counters and electromagnetic calorimeters. The drift chambers and time-of-flight scintillation counters covered in-plane scattering angles from about 8° to 140°, and the Cerenkov counters and electromagnetic calorimeters covered about 8° to 45°. The six sectors collectively covered 50–80% of the out-of-plane angle.

The positions of charged particles were measured in the drift chambers, allowing reconstruction of their trajectories as they bent, which was due to the influence of the toroidal magnetic field. The charge of the charged particles (electrons and protons in this work) and their momenta were determined from their reconstructed trajectories. We consider only charged particles the trajectories of which were reconstructed to originate in the location of the solid target foil[31].

Electrons were distinguished from pions by requiring a large signal in the Cerenkov counters, as well as a large energy deposition, proportional to momentum, in the electromagnetic calorimeters. Protons were identified by requiring that their time of flight, measured by the scintillation counters, was within two standard deviations of the calculated time of flight based on the momentum reconstructed in the drift chambers, assuming the particle has the mass of a proton.

Measurement kinematics and reaction mechanism effects

Experimentally, we measured final-state particles and reconstructed the initial state of the nucleons (before the electron interaction), on the basis of modelling of the electron scattering reaction using the GCF to model the nuclear spectral and decay functions[9,15,17,22–25,32–34]. This work focuses on the specific interpretation of the data in terms of quasielastic electron scattering from a single nucleon, as shown in Extended Data Fig. 1. However, as shown by previous studies, the reaction can also include contributions from meson-exchange currents, isobar currents (exciting the struck nucleon to an intermediate excited state), elastic and inelastic nucleon rescattering (final-state interactions, FSIs), and single charge-exchange (SCX) reactions; all four can all lead to a similar final state as the quasielastic scattering reaction. The relative contribution of these reaction mechanisms depends on the kinematics of the experiment[17–19,35–39]; for a detailed discussion and review of previous experimental and theoretical studies see ref. [7,8] and references therein. For example, isobar currents are suppressed for $x_B > 1$, because for a given Q^2 the virtual photon transfers less energy and is less likely to excite the nucleon to a higher energy state.

For high-missing-momentum events, elastic FSIs include rescattering of the outgoing nucleon with the other nucleon of the SRC pair or with the other nucleons in the residual nucleus. At large knockout nucleon momenta, such rescattering (as well as SCX interactions), can be estimated using a generalized eikonal approximation in a Glauber framework[18,19,40], previously shown to give a good reproduction of experimental data[41–43]. These calculations show that in our kinematics, elastic FSIs are largely confined to nucleons in close proximity, and the largest part of the scattering cross-section can be attributed to rescattering between nucleons of the SRC pair[44]. Therefore, FSI predominantly leads to flux reduction that can be quantified in terms of a transparency factor.

SCX can turn proton knockout events into neutron knockout events (reducing the measured proton yield), as well as turn neutron knockout events into proton knockout events (increasing the measured proton yield). The rate of both (p, n) and (n, p) SCX can similarly be quantified by probability factors.

In addition, rescattering between the knockout and recoil nucleons (that is, the nucleons of the pair) can also distort the kinematics of the measured events. Previous studies of the deuteron show that, in the kinematics of the current measurement, such internal pair rescattering is strongly suppressed[39].

Thus, the two main reaction mechanisms that effect our measurement are reductions in the measured cross-section owing to transparency, and SCX-induced enhancements resulting from neutron knockout interactions.

One should note that this simple quasielastic picture, with suppressed elastic FSIs, is strongly supported by the fact that it describes well both high-Q^2 electron-scattering data and high-energy proton-scattering data[15,45], which have very different reaction mechanisms. In addition, the results of the electron- and proton-scattering experiments give consistent SRC-pair isospin ratios[10,13,15] and centre-of-mass momentum distributions[16,45,46].

Non-quasielastic reaction mechanisms such as small-angle leading-nucleon rescattering can modify the measured kinematics. By changing the leading-nucleon momentum, rescattering can cause events with high missing momentum that originate from interactions with low-initial-momentum nucleons. These effects are not accounted for by the SCX and transparency corrections detailed below and can therefore interfere with the interpretation of the data.

Such effects have characteristic kinematics and are expected to increase with nuclear size (that is, the effects are expected to be more noticeable for heavier nuclei). As detailed in Supplementary Information, we do not observe the expected characteristic behaviours and do observe that the data measured for different nuclei are very similar (see Extended Data Figs. 2, 3). This indicates that A-dependent effects are small and that our data are not substantially distorted by re-scattering effects that go beyond transparency and SCX. See Supplementary Information for details.

GCF model: input parameters, reaction mechanism corrections and comparison with experimental data

The GCF cross-section model and its calculation method are detailed in Supplementary Information. Here we discuss the model input parameters, corrections for FSI and SCX effects and assessment of the model systematic uncertainty.

The GCF cross-section calculation requires four external inputs.

Nuclear contact values (C^{α}_{NN}). For the AV18, AV4′ and N2LO interaction models we use nuclear contacts that were previously extracted from analyses of two-nucleon momentum distributions[24,25], obtained from many-body quantum Monte Carlo calculations for carbon[47,48]. Because we normalize the simulated event yields to the integrated number of $(e, e'p)$ data events, our calculations are only sensitive to the relative values of the contacts.

Universal $\tilde{\varphi}^{\alpha}_{12}(p_{12})$ functions. These are taken as the solution of the two-body Schrodinger equation for a nucleon pair (1, 2) with quantum numbers α; see refs. [23–25] for details. $\tilde{\varphi}^{\alpha}_{12}(p_{12})$ are nucleus-independent, but depend on the *NN* interaction model used in its calculation. In the case of the spin-1 ($s = 1$) quantum state this amounts to the deuteron wavefunction shown in Extended Data Fig. 6a. For the spin-0 ($s = 0$) quantum state it is the zero-energy solution of the two-body *NN* system, see Extended Data Fig. 6b for the *pp* channel.

Centre-of-mass momentum distributions of SRC pairs. These distributions were studied both theoretically[49,50] and experimentally[11,16,45,46] and were found to be well described by a three-dimensional Gaussian that is defined by its width. For the nuclei considered here, both measurements and theoretical calculations show this width to be about 150 ± 20 MeV/c (ref. [16]).

Excitation energy of the $A-2$ system, E^{*}_{A-2}. Unlike the other inputs mentioned above, E^{*}_{A-2} has not been measured before and can therefore take any value up to about the Fermi energy (roughly 30 MeV).

The comparison of the GCF model with experimental data was done using Monte Carlo integration. We implemented the GCF cross-section model (both the regular and light-cone versions[9,15,51–53]) in an event generator that simulates the reaction shown in Extended Data Fig. 1, in which an electron has a hard scattering from a nucleon in an SRC pair within a nucleus, causing both the struck nucleon and the correlated partner nucleon to be ejected from the nucleus. Events are weighted by the GCF cross-section and we account for electron radiation effects using the peaking approximation[54], in which the radiated photon is emitted in the direction of either the incoming or outgoing electron. See Supplementary Information for details.

To compare our event generator to data, we take the following steps. First, the Monte Carlo events are generated as explained above, and the weight of each event is multiplied by the CLAS detection efficiency for the particles detected in that event. Second, the generated electron and proton momenta are smeared to account for the CLAS resolution, and events with particles that would not have been detected are rejected. Finally, we apply the same event-selection cuts used to select the data events.

We accounted for transparency and SCX by constructing the following relations[13,18] for the experimental $(e,e'p)$ and $(e,e'pp)$ events

$$\sigma^{\mathrm{exp}}_{\mathrm{A}(e,e'pp)} = \sigma^{\mathrm{GCF}}_{\mathrm{A}(e,e'pp)} P^{pp}_{\mathrm{A}} T^{NN}_{\mathrm{A}} + \sigma^{\mathrm{GCF}}_{\mathrm{A}(e,e'np)} P^{[n]p}_{\mathrm{A}} T^{NN}_{\mathrm{A}} + \sigma^{\mathrm{GCF}}_{\mathrm{A}(e,e'pn)} P^{p[n]}_{\mathrm{A}} T^{NN}_{\mathrm{A}}$$

$$\begin{aligned}\sigma^{\mathrm{exp}}_{\mathrm{A}(e,e'p)} = {} & (\sigma^{\mathrm{GCF}}_{\mathrm{A}(e,e'pp)} + \sigma^{\mathrm{GCF}}_{\mathrm{A}(e,e'pn)}) P^{pp}_{\mathrm{A}} T^{N}_{\mathrm{A}} + \sigma^{\mathrm{GCF}}_{\mathrm{A}(e,e'np)} P^{[n]p}_{\mathrm{A}} T^{N}_{\mathrm{A}} \\ & + \sigma^{\mathrm{GCF}}_{\mathrm{A}(e,e'nn)} P^{[n]n}_{\mathrm{A}} T^{N}_{\mathrm{A}}\end{aligned} \quad (2)$$

where $\sigma^{\mathrm{GCF}}_{X}$ (or $\sigma^{\mathrm{exp}}_{X}$) are the GCF simulated (or experimental) events for a process X without FSI or SCX, and the P_{A} and T_{A} factors are multiplied to the event weights to account for SCX and transparency probabilities, respectively. The P_{A} and T_{A} factors do not affect the kinematics of the calculated events.

T^{NN}_{A} refers to the transparency of both the leading and recoil nucleons that are emitted simultaneously, whereas T^{N}_{A} refers to the transparency for the leading nucleon, independent of the recoil nucleon. We assume that the transparencies for protons and neutrons are the same, and are therefore independent of SCX.

As SCX probabilities are different for protons and neutrons and for high and low momentum, the superscript notation in the P factor represents the exact process being considered, such that particle with (without) square brackets is the one that undergoes (does not undergo) SCX. For example, $P^{[p]p}_{\mathrm{A}}$ is the probability that a leading proton in a pp pair undergoes SCX, $P^{p[p]}_{\mathrm{A}}$ is this probability for the recoil proton and $P^{pp}_{\mathrm{A}} = 1 - P^{[p]p}_{\mathrm{A}} - P^{p[p]}_{\mathrm{A}}$ is the probability that no proton undergoes SCX. As can be seen, SCX changes final-state neutrons to protons and vice versa. We neglect cases in which more than one particle undergoes SCX, as these have negligible probability.

The values used for these probabilities are listed in Supplementary Information Table 1. They are based on Glauber calculations[18], which agree well with experimental data[41–43]. Both the Glauber calculations and the data show that, for the kinematics of the current measurements, these probabilities are energy-independent for the leading nucleon. The transparency of the leading nucleon forces the $(e,e'pp)$ reaction to take place near the nuclear surface, such that the energy dependence of the transparency of the recoil nucleon is also expected to be very small. As these effects are model-dependent, we chose to include them in the calculated cross-sections, leaving the data fully model-independent.

GCF model: systematic uncertainties

Uncertainty on the GCF and event-generator input parameters (for example, CLAS resolution factors, transparency factors, SCX probabilities, nuclear contacts, centre-of-mass motion of the SRC pair, $A-2$ system excitation energy, and the relative momentum value of the pair for the onset of the SRC regime) all contribute to the total systematic uncertainty of the calculation. We accounted for this uncertainty by simulating a large number of 'universes', in which the uncertain input parameters are each randomly drawn from prior probability distributions. We then examined the spread of the generator results across this space of 'universes' to produce a systematic uncertainty band that captures 1σ of the examined parameter combinations.

The following values and Gaussian uncertainties were used for these parameters for ^{12}C: σ_{CM}, the Gaussian width of the centre-of-mass momentum distribution of the SRC pair[16], was 150 ± 20 MeV/c; the nuclear contacts for AV18, AV4′ and N2LO were taken from ref. [25], specifically the k-space fits in table 1 of the supplementary materials therein; and the SCX and nuclear transparency probabilities and uncertainties were from ref. [13] (see Supplementary Information Table 1). Then, E^{*}_{A-2}, the excitation energy of the residual $A-2$ system, was varied uniformly between 0 and 30 MeV; the $p^{\mathrm{min}}_{\mathrm{rel}}$ cut off in the universal two-body functions was varied uniformly between 250 and 350 MeV/c; the simulated electron resolution was varied uniformly between 1.0% and 1.5%; the simulated proton resolution was varied uniformly between 0.8% and 1.2%; and the off-shell electron–nucleon cross-section was chosen to be either[21] σ_{CC1} or σ_{CC2}.

We note that although the individual parameter uncertainties are independent of each other, their impact on the calculated cross-section can be correlated. For example, both E^{*}_{A-2} and σ_{CM} can affect the initial pair energy in a similar manner (Extended Data Fig. 1). By varying all parameters simultaneously we include the effects of such correlations. We also note that the use of σ_{CC1} versus σ_{CC2} is a discrete choice, in contrast to all the other variations, which are continuous. We compared the calculations done using only σ_{CC1} and only σ_{CC2} and did not see a considerable difference in the resulting distributions.

Initial nucleon energy

We use the convention that the spectral function depends on ϵ_{i}, the initial off-shell energy of the struck nucleon before scattering. The expected initial off-shell energy for nucleons in a stationary pair is given by:

$$\epsilon_{\mathrm{i}} = m_A - m_{A-2} - \sqrt{p_{\mathrm{i}}^2 + m_N^2} \quad (3)$$

which is shown by red arrows in Fig. 3 and Extended Data Fig. 7d–k.

Estimation of the scalar limit

The general expectation for a fully scalar NN interaction and a symmetric nucleus is that the abundance of pairs will be equal for all isospin, spin and spin-projection states. This implies that the number of spin-1 pn SRC pairs should be three times the number of spin-0 pp, pn and nn pairs, owing to the three possible spin orientations. Therefore, simple counting (indicated by '#') implies that the scalar limit is:

$$\frac{\#\mathrm{A}(e'pp)}{\#\mathrm{A}(e'p)} = \frac{2N^{s=0}_{pp}}{2N^{s=0}_{pp} + N^{s=0}_{pn} + N^{s=1}_{pn}} = \frac{2N^{s=0}}{(2+1+3)N^{s=0}} = \frac{1}{3} \quad (4)$$

where $N^{s=S}_{NN}$ is the number of NN pairs in a spin-S state. This limit is shown as the horizontal dashed line in Extended Data Fig. 6c.

Cut-off dependence and non-local chiral interactions

In addition to the local interactions studied in this work, nuclear structure calculations are often performed using non-local interactions, which feature different higher-momentum asymptotic behaviour compared to local ones. The non-local versions of the χEFT interactions have momentum-space cut offs and are considered to be 'softer' than the local interactions studied here.

The main limitation for studying such interactions using the GCF framework presented here is that, at the moment, there are no available calculations of the two-nucleon momentum distribution in ^{12}C using these interactions. Therefore, we are unable to determine the nuclear

contacts for these interactions in a fully theoretical fashion as is done for the local interactions considered above.

One previous work[22] studied the non-local next-to-next-to-next-to-leading-order (N3LO) (600 MeV/c) interaction[5] using the GCF by extracting the ratio of spin-1 to spin-0 contacts from a fit to experimental data[10,11]. Although this procedure cannot be compared on an equal footing with the fully theoretical predictions we have for the local interactions, it is still interesting to see how they compare with each other and with the data. This comparison is shown in Extended Data Fig. 8, which is equivalent to Figs. 2a, 3a, b. As can be seen, the non-local N3LO (600 MeV/c) interaction seems to reproduce well the experimental data up to its cut off, but then decays faster than the local interactions. This is an encouraging observation, because the 600-MeV/c cut off of this interaction is well above the 300-MeV/c centre-of-mass momentum cut off of the *NN* phase-shift data used in its construction.

The predictions of the N3LO (600 MeV/c) interaction are quite similar to those of the N2LO (1.2 fm) interaction. This might seem surprising as the 1.2-fm cut off corresponds to momenta of[26,55] 400 MeV/c, smaller than 600 MeV/c and, as mentioned previously, one expects large errors in the predictions of the different χEFT interactions already at their cut-off scale. Our observations, consistent with theoretical expectations, indicate that for the processes studied here the nature of the position-space regulators makes their effects important only at a comparatively high momenta scale of 600–700 MeV/c; see Fig. 3d–i.

Future studies will focus on using the experimental data provided in this work (which are much more detailed than those produced previously[10,11]) to fit the nuclear contacts for different local and non-local interactions and study the dependence of the results on the chiral expansion order and cut off.

For completeness, we note that from a theoretical standpoint, the reaction diagram used for the GCF calculations (shown in Extended Data Fig. 1) can be viewed as a 'high-resolution' starting point for a unitary-transformed calculation[56]. As a thought exercise, the χEFT *NN* interactions used here can be considered as resulting from applying unitary transformations to models that have shorter distance and/or higher-momentum cut offs. As this process would introduce many-body interaction currents to the description of the electron scattering reaction, the use of a high-resolution (one-body) reaction description with χEFT interactions, as done in this work, is non-trivial. This is one explanation for the disagreement between the data and calculations at high p_{miss}. The data presented here can therefore quantify the importance of such many-body effects and demonstrate that they become important only above the cut off for non-relativistic calculations and at much higher momenta when relativistic effects are accounted for. This could help guide future studies of effects such as relativity and non-nucleonic degrees of freedom.

Fitting contact ratios to ($e, e'pp$)/($e, e'p$) data

In addition to using the ^{12}C contact values from ref. [25] to make GCF predictions, we also used the measured ($e, e'pp$)/($e, e'p$) data (Fig. 2b) to infer the ratio of spin-0 to spin-1 contacts, $C_{pp}^{s=0}/C_{pn}^{s=1}$, for each measured nucleus. We specifically used the ($e, e'pp$)/($e, e'p$) ratio because the cut-off effects largely cancel. We used Bayesian inference with the contact ratio as the sole parameter of interest. All other GCF parameters were treated as nuisance parameters and were integrated out, with prior distributions matching the systematic uncertainty sampling distributions described above. We assumed a scale-invariant prior on the ratio of interest, $C_{pp}^{s=0}/C_{pn}^{s=1}$. Additionally, we assume a ratio of spin-0 contacts, $C_{pp}^{s=0}/C_{pn}^{s=0}$, of 1 for carbon, aluminium and iron. For lead, this ratio was assumed to equal 82/126 = 0.65.

To evaluate the likelihood of the data for a given set of values of the GCF parameters, we multiplied the individual likelihoods of the 10 data points in Fig. 2b, assuming the data were distributed normally. The posterior distribution was determined by scanning over $C_{pp}^{s=0}/C_{pn}^{s=1}$ and Monte Carlo integrating over all nuisance parameters at each step.

The results are presented in Extended Data Table 1. The central value is the maximum (mode) of the posterior distribution, and the uncertainty intervals are the smallest intervals containing 68.3% (1σ) and 95.5% (2σ) of the total posterior. The table also shows the double ratio of contacts for the nuclei A relative to carbon, which is independent of the *NN* interaction model[25].

Data availability

The raw data from this experiment are archived in Jefferson Lab's mass storage silo.

31. Hakobyan, H. et al. A double-target system for precision measurements of nuclear medium effects. *Nucl. Instrum. Meth. A* **592**, 218–223 (2008).
32. Cruz-Torres, R. et al. Short-range correlations and the isospin dependence of nuclear correlation functions. *Phys. Lett. B* **785**, 304–308 (2018).
33. Weiss, R., Schmidt, A., Miller, G. A. & Barnea, N. Short-range correlations and the charge density. *Phys. Lett. B* **790**, 484–489 (2019).
34. Sargsian, M. M., Abrahamyan, T. V., Strikman, M. I. & Frankfurt, L. L. Exclusive electrodisintegration of ^{3}He at high Q^2. II. Decay function formalism. *Phys. Rev. C* **71**, 044615 (2005).
35. Frankfurt, L. L., Sargsian, M. M. & Strikman, M. I. Feynman graphs and generalized eikonal approach to high energy knock-out processes. *Phys. Rev. C* **56**, 1124–1137 (1997).
36. Rvachev, M. et al. Quasielastic ^{3}He($e, e'p$)^{2}H reaction at Q^2 = 1.5 GeV^2 for recoil momenta up to 1 GeV/c. *Phys. Rev. Lett.* **94**, 192302 (2005).
37. Benmokhtar, F. et al. Measurement of the ^{3}He($e, e'p$)pn reaction at high missing energies and momenta. *Phys. Rev. Lett.* **94**, 082305 (2005).
38. Egiyan, K. S. et al. (CLAS Collaboration) Experimental study of exclusive ^{2}H($e, e'p$)n reaction mechanisms. *Phys. Rev. Lett.* **98**, 262502 (2007).
39. Boeglin, W. U. et al. Probing the high momentum component of the deuteron at high Q^2. *Phys. Rev. Lett.* **107**, 262501 (2011).
40. Dutta, D., Hafidi, K. & Strikman, M. Color transparency: past, present and future. *Prog. Part. Nucl. Phys.* **69**, 1–27 (2013).
41. The CLAS Collaboration. Measurement of transparency ratios for protons from short-range correlated pairs. *Phys. Lett. B* **722**, 63–68 (2013).
42. The CLAS Collaboration. Measurement of nuclear transparency ratios for protons and neutrons. *Phys. Lett. B* **797**, 134792 (2019).
43. Colle, C. et al. Extracting the mass dependence and quantum numbers of short-range correlated pairs from A($e, e'p$) and A($e, e'pp$) scattering. *Phys. Rev. C* **92**, 024604 (2015).
44. Ciofi degli Atti, C. & Morita, H. Universality of many-body two-nucleon momentum distributions: correlated nucleon spectral function of complex nuclei. *Phys. Rev. C* **96**, 064317 (2017).
45. Tang, A. et al. (EVA Collaboration) n–p short-range correlations from (p, 2p + n) measurements. *Phys. Rev. Lett.* **90**, 042301 (2003).
46. Shneor, R. et al. (Jefferson Lab Hall A Collaboration) Investigation of proton–proton short-range correlations via the ^{12}C($e, e'pp$) reaction. *Phys. Rev. Lett.* **99**, 072501 (2007).
47. Lonardoni, D., Gandolfi, S., Wang, X. B. & Carlson, J. Single- and two-nucleon momentum distributions for local chiral interactions. *Phys. Rev. C* **98**, 014322 (2018).
48. Wiringa, R. B., Schiavilla, R., Pieper, S. C. & Carlson, J. Nucleon and nucleon-pair momentum distributions in $A \leq 12$ nuclei. *Phys. Rev. C* **89**, 024305 (2014).
49. Ciofi degli Atti, C. & Simula, S. Realistic model of the nucleon spectral function in few and many nucleon systems. *Phys. Rev. C* **53**, 1689–1710 (1996).
50. Colle, C., Cosyn, W., Ryckebusch, J. & Vanhalst, M. Factorization of exclusive electron-induced two-nucleon knockout. *Phys. Rev. C* **89**, 024603 (2014).
51. Frankfurt, L. & Strikman, M. Short-range correlations in nuclei as seen in hard nuclear reactions and light cone dynamics. In *Modern Topics in Electron Scattering* (eds Frois, B. & Sick, I.) 645–694 (1992).
52. Artiles, O. & Sargsian, M. Multinucleon short-range correlation model for nuclear spectral functions: theoretical framework. *Phys. Rev. C* **94**, 064318 (2016).
53. Miller, G. A. & Tiburzi, B. C. Relation between equal-time and light-front wave functions. *Phys. Rev. C* **81**, 035201 (2010).
54. Ent, R. et al. Radiative corrections for ($e, e'p$) reactions at GeV energies. *Phys. Rev. C* **64**, 054610 (2001).
55. Lynn, J. E. et al. Quantum Monte Carlo calculations of light nuclei with local chiral two- and three-nucleon interactions. *Phys. Rev. C* **96**, 054007 (2017).
56. More, S. N., Bogner, S. K. & Furnstahl, R. J. Scale dependence of deuteron electrodisintegration. *Phys. Rev. C* **96**, 054004 (2017).

Acknowledgements We acknowledge the efforts of the staff of the Accelerator and Physics Divisions at Jefferson Lab that made this experiment possible. The analysis presented here was carried out as part of the Jefferson Lab Hall B data-mining project supported by the US Department of Energy (DOE). The research was also supported by the National Science Foundation, the Israel Science Foundation, the Pazi Foundation, the Chilean Comisión Nacional de Investigación Científica y Tecnológica, the French Centre National de la Recherche Scientifique and Commissariat a l'Energie Atomique, the French–American Cultural Exchange, the Italian Istituto Nazionale di Fisica Nucleare, the National Research Foundation of Korea, and the UK Science and Technology Facilities Council. Jefferson Science Associates operates the Thomas Jefferson National Accelerator Facility for the DOE, Office of Science, Office of Nuclear Physics under contract DE-AC05-06OR23177.

Author contributions The CEBAF Large Acceptance Spectrometer was designed and constructed by the CLAS Collaboration and Jefferson Lab. Data acquisition, processing

and calibration, Monte Carlo simulations of the detector and data analyses were performed by a large number of CLAS Collaboration members, who also discussed and approved the scientific results. The analysis presented here was performed primarily by A.S. and J.R.P. R. Weiss and N.B. provided theoretical input and helped implement parts of the GCF event generator. M.S. and A.L. provided theoretical input and helped implement the light-cone formalism. A. Denniston and E.P.S. helped implement parts of the GCF event generator and performed the model systematic uncertainty studies. A.H. calculated the CLAS acceptance maps. O.H., E. Piasetzky, and L.B.W. guided and supervised the analysis.

Competing interests The authors declare no competing interests.

Additional information

Supplementary information is available for this paper at https://doi.org/10.1038/s41586-020-2021-6.

Correspondence and requests for materials should be addressed to O.H.

Peer review information *Nature* thanks Daniel Phillips and the other, anonymous, reviewer(s) for their contribution to the peer review of this work.

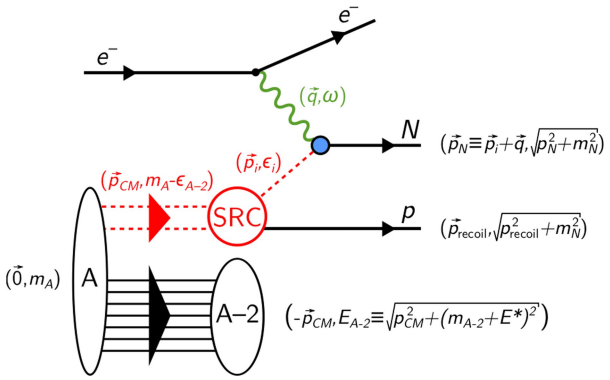

Extended Data Fig. 1 | SRC pair breakup. Diagrammatic representation and four-momentum kinematics of the two-nucleon knockout A($e, e'Np$) reaction within the SRC model. The dashed red lines represent off-shell particles and solid black lines represent detected particles. The $A-2$ system is undetected.

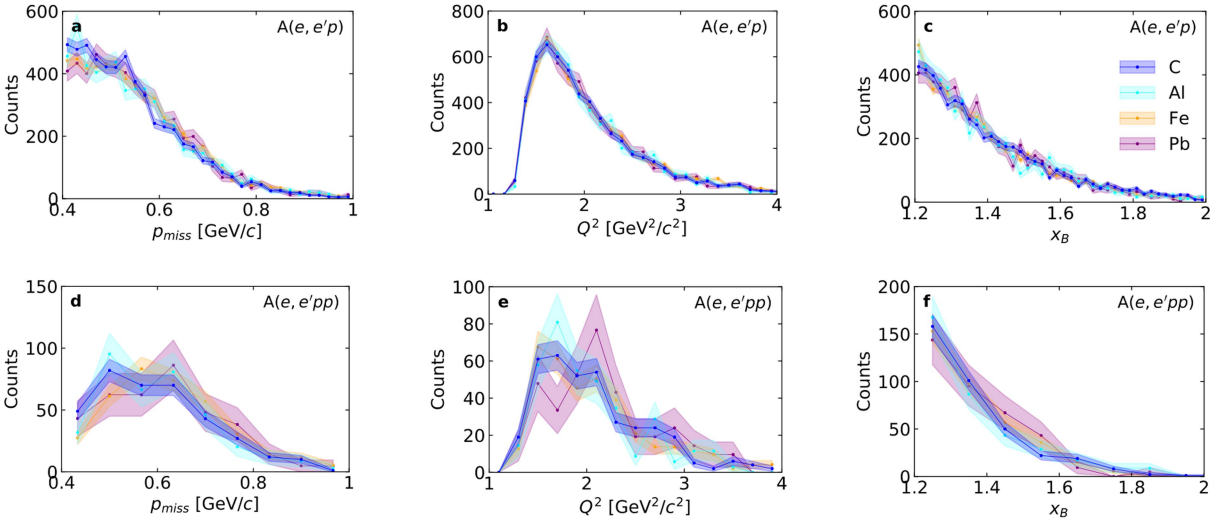

Extended Data Fig. 2 | Kinematical distributions and A(*e*, *e'pp*)/A(*e*, *e'p*) ratios for *A* = 12–208 nuclei. a–**c**, Comparison of the number of A(*e*, *e'p*) event reactions versus the (*e*, *e'p*) missing momentum p_{miss} (**a**), Q^2 (**b**) and x_{B} (**c**). **d**–**f**, Comparison of the number of A(*e*, *e'pp*) event reactions versus the (*e*, *e'p*) missing momentum p_{miss} (**d**), Q^2 (**e**) and x_{B} (**f**). The total number of counts in aluminium (cyan), iron (orange), and lead (purple) was scaled to match that of carbon (dark blue). The shaded bands indicate the 1σ statistical uncertainty of the data.

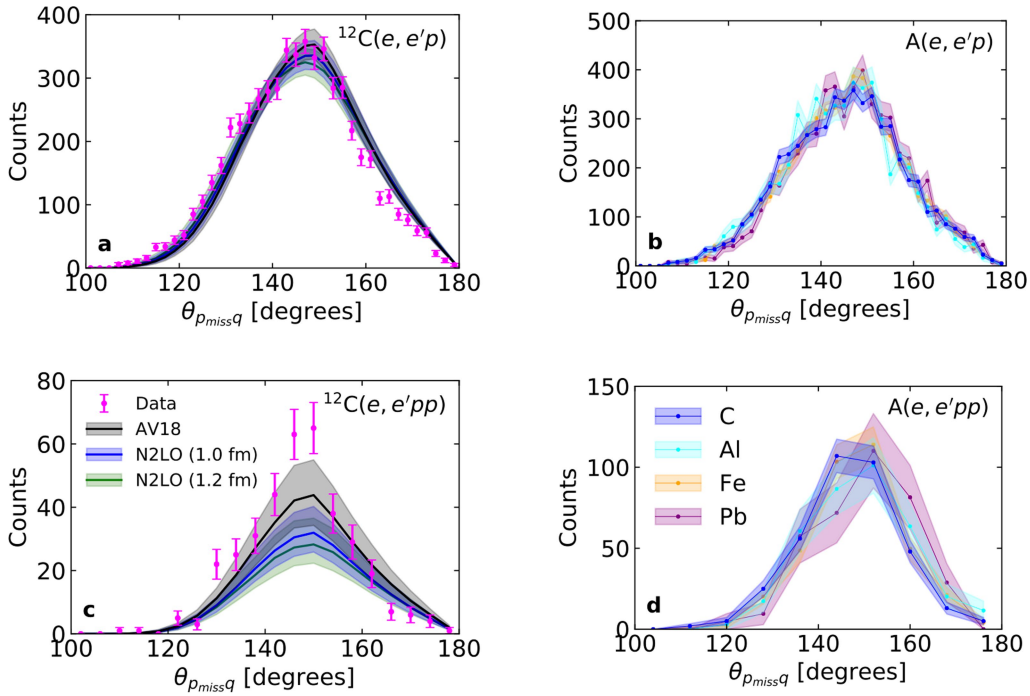

Extended Data Fig. 3 | Momentum-transfer and missing-momentum angular correlations. a–**d**, Distribution of the relative angle between the momentum transfer **q** and the (*e*, *e′p*) missing momentum for A(*e*, *e′p*) (**a**, **b**) and A(*e*, *e′pp*) (**c**, **d**). The panels at left compare the ^{12}C data and GCF calculations using different *NN* interaction models (**a**, **c**); and the panels at right compare the data for carbon (blue), aluminium (cyan), iron (orange), and lead (purple) nuclei (**b**, **d**). The total number of counts in the aluminium, iron and lead data has been scaled to match that of carbon. In **a** and **c**, the width of the band and the data error bars show the model systematic uncertainties and data statistical uncertainties, respectively, each at the 1σ confidence level. The shaded bands in **b** and **d** indicate the 1σ statistical uncertainty of the data.

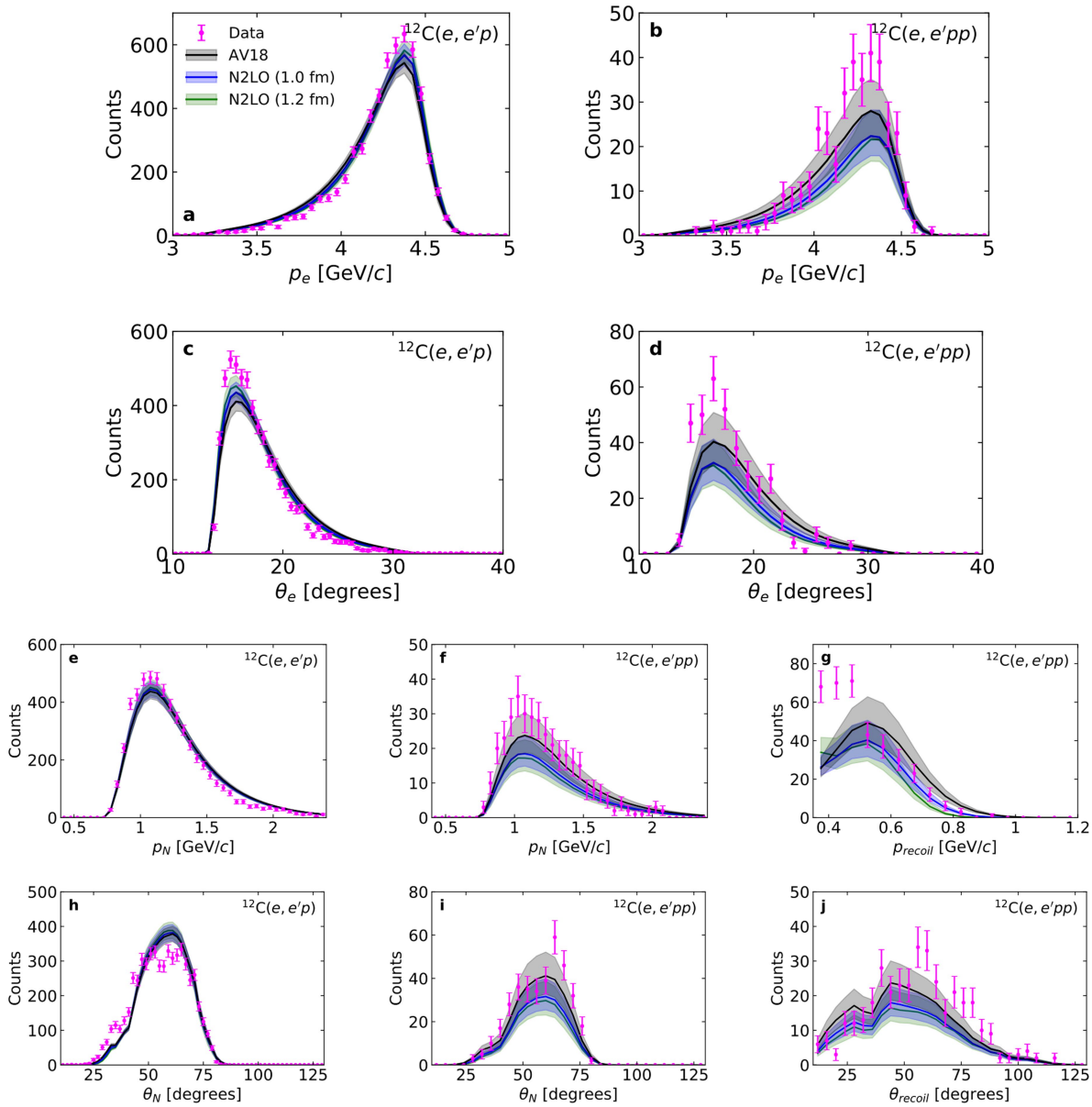

Extended Data Fig. 4 | Electron and proton kinematics. Momentum and angle distributions of scattered electrons and protons for ^{12}C(*e*, *e*′*p*) (**a**, **c**, **e**, **h**) and ^{12}C(*e*, *e*′*pp*) (**b**, **d**, **f**, **g**, **i**, **j**) events. Coloured bands show the various GCF calculations. The width of the shaded band and the data error bars show the model systematic uncertainties and data statistical uncertainties, respectively, each at the 1σ confidence level.

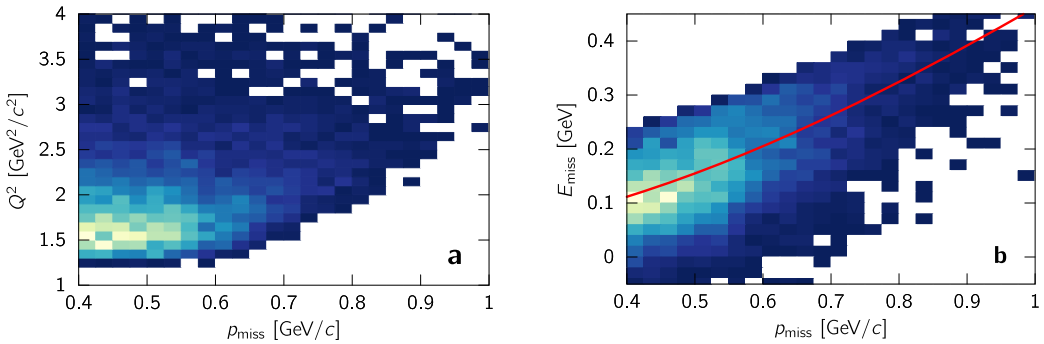

Extended Data Fig. 5 | Kinematic correlations of ^{12}C($e, e'p$) events. a, Q^2 versus the missing-momentum distribution of ^{12}C($e, e'p$) data. Owing to the event selection criteria, as p_{miss} approaches 1 GeV/c, the minimum Q^2 of the data approaches 3 GeV/c. **b**, E_{miss} versus p_{miss} of the ^{12}C($e, e'p$) data. The red line indicates the expected E_{miss}–p_{miss} correlation for the breakup of a stationary pair.

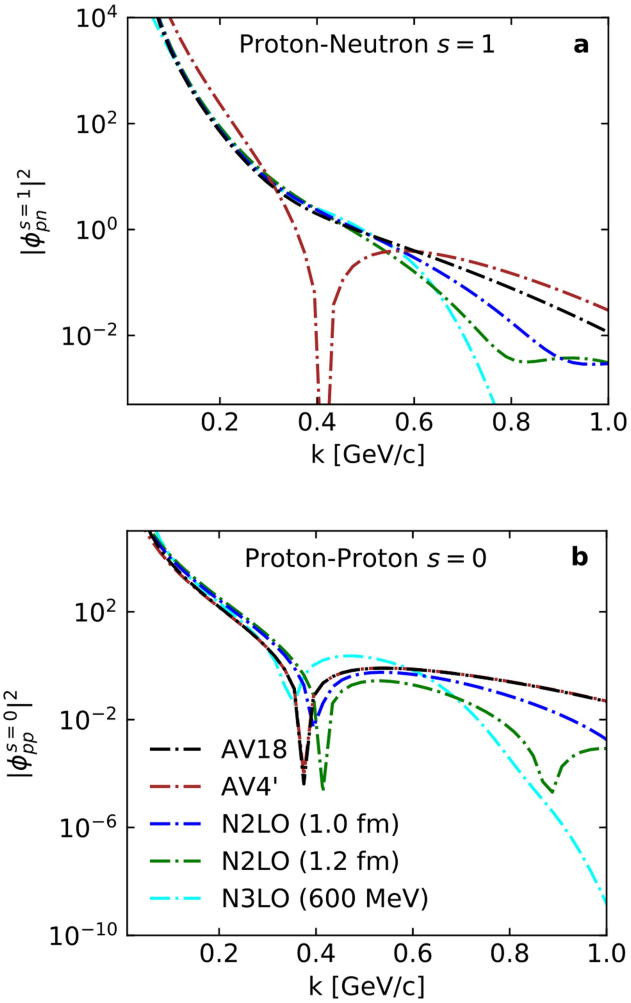

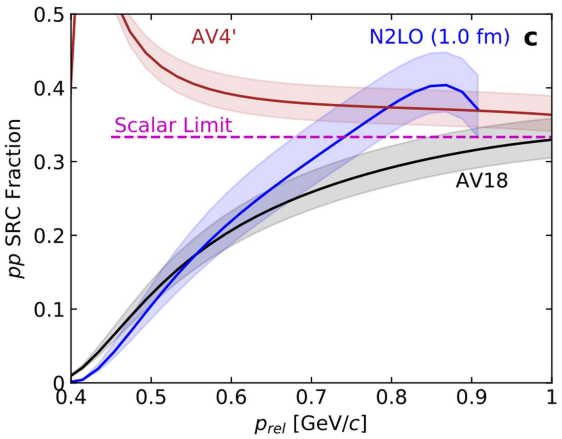

Extended Data Fig. 6 | Universal functions for *pp* and *np* pairs and the momentum dependence of their ratio. The relative momentum distributions for different *NN* interaction models studied in this work, for *pn* (**a**) and *pp* (**b**). **c**, The momentum dependence of the fraction of protons belonging to *pp* SRC pairs in ^{12}C.

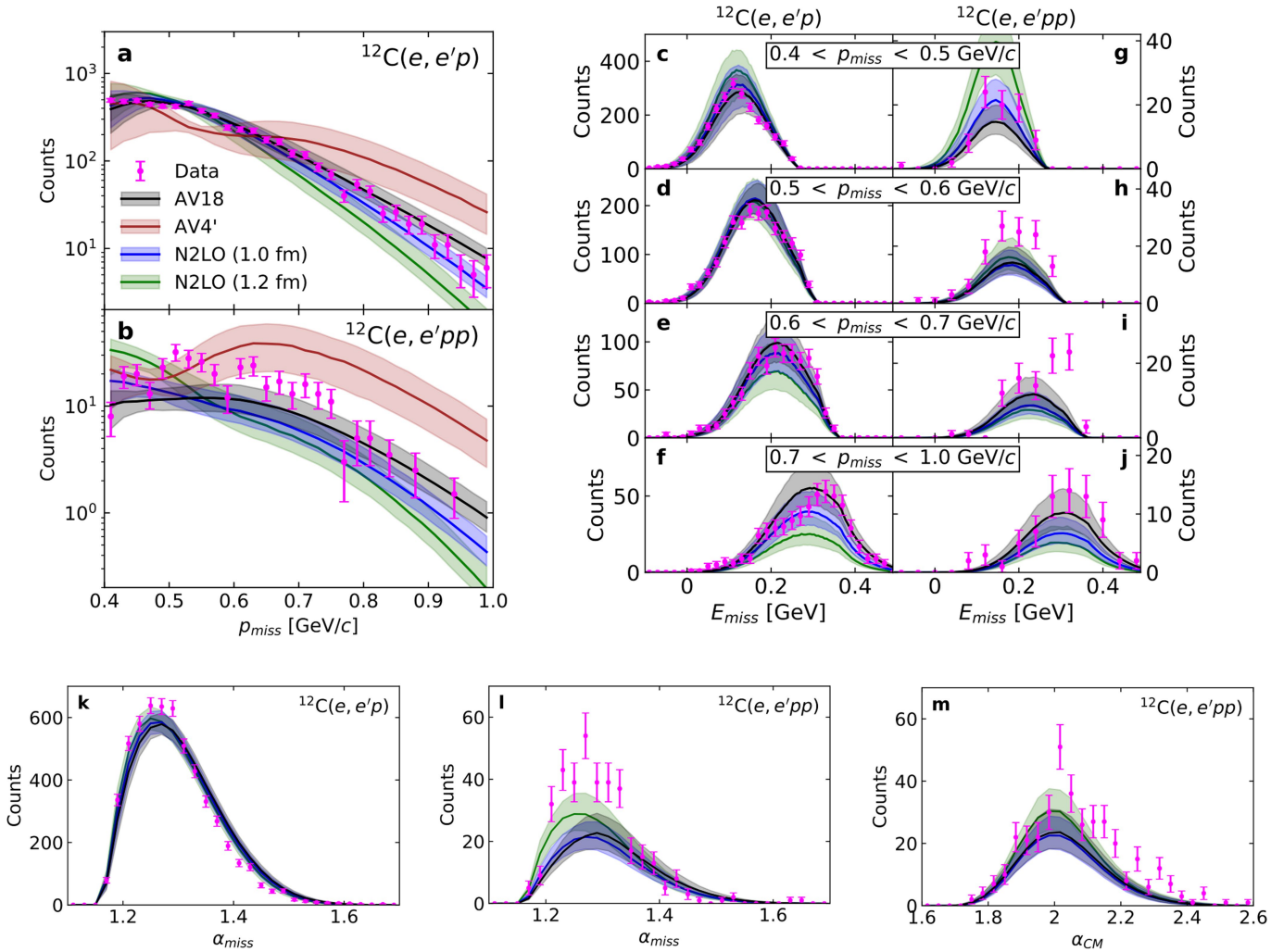

Extended Data Fig. 7 | Light-cone calculations of the nuclear spectral function and momentum fractions. a–j, As in Fig. 3a–j. **k**, **l**, The reconstructed initial light-cone momentum fraction carried by the struck nucleon for (*e*, *e′p*) (**k**) and (*e*, *e′pp*) (**l**) events. **m**, The total pair light-cone momentum fraction for (*e*, *e′pp*) events. The data points are identical to those in Fig. 3a–j. The bands are different and show the results of the GCF calculations using light-cone formalism and various *NN* interaction models. The width of the shaded band and the data error bars show the model systematic uncertainties and data statistical uncertainties, respectively, each at the 1σ confidence level.

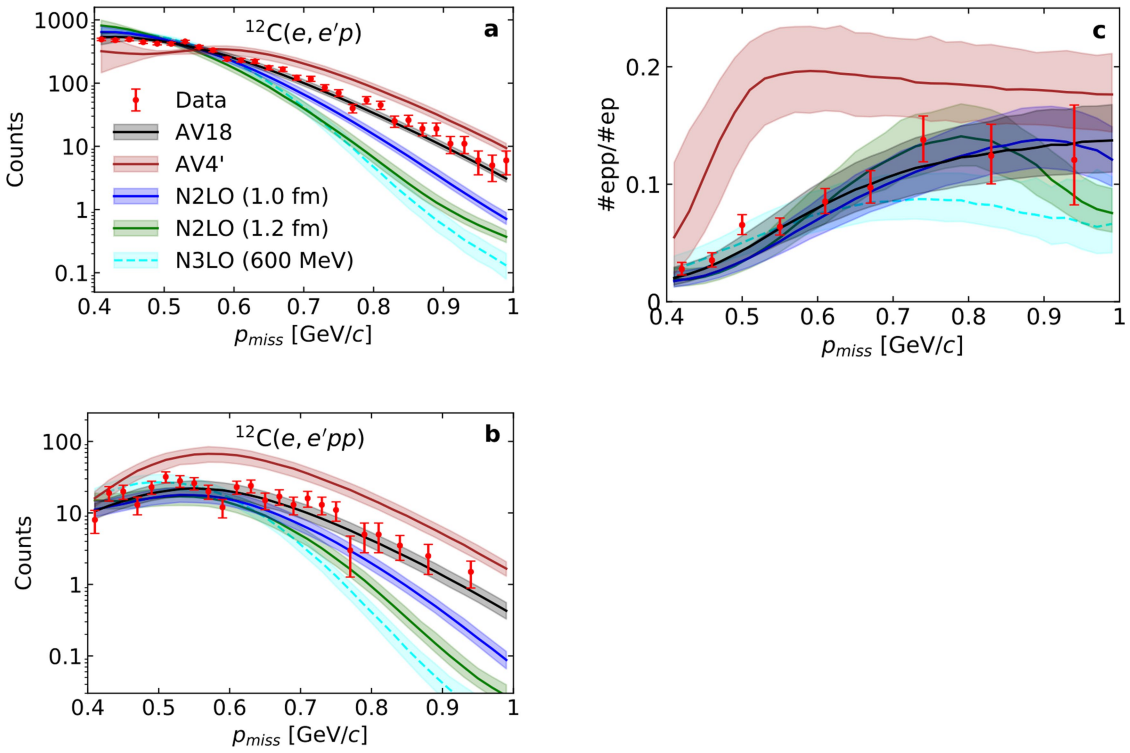

Extended Data Fig. 8 | Scale dependence and non-local interactions. a–**c**, As in Fig. 3a, b (**a**, **b**) and Fig. 2a (**c**), but also including the non-local N3LO (600 MeV/*c*) interaction. The width of the shaded band and the data error bars show the model systematic uncertainties and data statistical uncertainties, respectively, each at the 1σ confidence level. See Methods for details.

Extended Data Table 1 | Extracted contact ratios $C_{pp}^{s=0}/C_{np}^{s=1}$ for different nuclei

Interaction	^{12}C		^{27}Al [%]	Al/C	^{56}Fe [%]	Fe/C	^{208}Pb [%]	Pb/C
	This Work [%]	Ref. [25]						
AV18	$6.7^{+1.7\ (4.7)}_{-1.0\ (1.7)}$	7.2±1.6	$4.5^{+1.9\ (7.0)}_{-1.0\ (1.5)}$	0.67	$6.4^{+1.7\ (4.8)}_{-1.0\ (1.8)}$	0.96	$1.4^{+0.9\ (3.0)}_{-0.5\ (0.7)}$	0.21
N2LO (1.0 fm)	$8.1^{+2.8\ (9.7)}_{-1.4\ (2.3)}$	8.2±1.2	$5.3^{+2.7\ (11.3)}_{-1.2\ (2.0)}$	0.65	$8.0^{+2.8\ (9.2)}_{-1.5\ (2.4)}$	0.99	$1.8^{+1.2\ (4.4)}_{-0.6\ (0.8)}$	0.22
N2LO (1.2 fm)	$15.1^{+4.4\ (13.6)}_{-2.5\ (4.1)}$	18.7±2.8	$9.7^{+4.3\ (14.2)}_{-2.2\ (3.5)}$	0.64	$13.2^{+5.0\ (11.5)}_{-2.5\ (4.0)}$	0.87	$3.6^{+2.1\ (6.4)}_{-1.2\ (1.8)}$	0.24

Extracted by fitting the GCF calculation to the A(*e*, *e*′*pp*)/A(*e*, *e*′*p*) data shown in Fig. 2b.
Uncertainties are shown at the 1σ confidence level, followed by the 2σ uncertainty in parenthesis.